Geometric optics analysis of inverted graded index fibers

To cite this article: Joseba Zubia *et al* 2022 *J. Opt.* **24** 115602

View the article online for updates and enhancements.

You may also like

Geometric optics analysis of inverted graded index fibers

Joseba Zubia[1,*] , **Gotzon Aldabaldetreku**[1] , **Gaizka Durana**[1]
and María Asunción Illarramendi[2]

[1] Department of Communications Engineering, School of Engineering of Bilbao, University of the
Basque Country UPV/EHU, E-48013 Bilbao, Spain
[2] Department of Applied Physics, School of Engineering of Bilbao, University of the Basque Country
UPV/EHU, E-48013 Bilbao, Spain

E-mail: joseba.zubia@ehu.eus

CrossMark

Abstract
We derive a general solution based on geometric optics that describes the light propagation
properties in multimode optical fibers with inverted refractive index profiles. Using this general
solution, we classify rays according to their propagation properties and calculate the analytical
expressions of the ray trajectories inside these fibers under different launching conditions. In
addition, we discuss the most suitable propagation conditions that maximize the confinement of
light power in the vicinity of the core-cladding interface for sensing purposes.

Keywords: optical fibers, inverted graded index fibers, ray propagation, geometric optics

(Some figures may appear in colour only in the online journal)

1. Introduction

Although an accurate study of light propagation in optical
fibers would require solving Maxwell's equations [1], it is pos-
sible to make use of approximations based on geometric optics
if highly multimode fibers are involved. This approach has suc-
cessfully been applied to step-index and graded-index fibers
[2–6], as well as to more recent multi-step [7] and multicore
[8] fibers.

In 1991, Lachance and Bélanger proposed a new type of
fiber with a core of divergent parabolic graded-index pro-
file, a special fiber whose refractive index increased from the
fiber axis to the core-cladding interface [9]. Even though they
investigated the characteristics of such fibers by means of an
electromagnetic treatment, their analysis pertained only to the

fundamental mode. Likewise, other authors also tackled the
problem of solving Maxwell's equations in these fibers; how-
ever, their analyses were restricted to few propagating modes
[10, 11].

In 1998, Matejec *et al* revisited the subject and fabricated
inverted graded index (IGI) fibers [12]. A few years later,
Tsukada *et al* succeeded in manufacturing IGI fibers from
polymers [13]. Consequently, there is a renewed interest in
the study of these fibers because of their potential use in light
amplification and in the design of chemical sensors through the
evanescent field [14–19]. Likewise, IGI fibers are expected to
play a key role in the development of solar energy technolo-
gies and boost the transition towards clean energy, since the
manufacture of inverted graded index polymer optical fibers
with embedded photo luminescent entities will enable their
use as luminescent solar concentrators [20, 21]. For instance,
in IGI fibers featuring a radially-growing dopant distribution
(dyes, quantum dots, doped-scattering nanoparticles or any
efficient combination of them), most of the dopants accu-
mulate in the proximity of the fiber-air interface, facilitating
the absorption of sunlight and its subsequent re-emission as
fluorescence light that is collected in the fiber ends, where

---

* Author to whom any correspondence should be addressed.

the photovoltaic cells are placed for the energy conversion [22–24].

Even though the propagation of rays in a meridional plane has been explained to a considerable extent, to the best of our knowledge, there is still missing a general solution that includes the whole set of rays in an IGI fiber. The problem of solving ray paths can be addressed by making use of different formalisms, yet equivalent. Among others, we can highlight the Eikonal or ray equation [25] as well as the Lagrangian and Hamiltonian formalisms [26, 27]. Because of the simplicity of the solutions obtained from the Eikonal equation and since this approach provides an adequate framework to identify symmetries and invariants, we have obtained the general solution of ray propagation in a multimode IGI fiber from the Eikonal equation and using geometric optics.

In the following section, we will introduce the structure of the IGI fiber and classify rays depending on their oscillating or evanescent nature. Afterwards, we will solve the general equation for a ray path from the Eikonal equation and show some meaningful results obtained under specific conditions; in addition, we will discuss the most remarkable features and conditions that make these fibers especially suitable for sensing purposes and solar energy applications. Finally, we will summarize the main conclusions.

2. Theory

2.1. Description of the fiber

We will focus on the study of light propagation in IGI fibers with the following refractive index profile:

$$n^2(r) = \begin{cases} n_o^2 \left[1 + 2\Delta \left(\dfrac{r}{\rho} \right)^2 \right] & r \leqslant \rho, \\ n_{cl}^2 & r > \rho, \end{cases} \quad (1)$$

where n_o is the refractive index on the fiber axis, n_{cl} the refractive index of the surrounding cladding material, ρ the half of the fiber core diameter $d = 2\rho$, and Δ the *inverted* profile height parameter defined as

$$\Delta = \frac{n_{co}^2 - n_o^2}{2n_o^2}, \quad (2)$$

being n_{co} the maximum value of the refractive index inside the core at the core-cladding interface $r = \rho$ (not to be confused with the standard profile height parameter used in conventional fibers).

The refractive index profile of equation (1) corresponds to a power-law profile, although the radial variation is inverted, in the sense that the refractive index increases as we move away from the fiber axis, reaching a maximum value n_{co} at the core-cladding interface. In the cladding, the refractive index is uniform and equal to n_{cl}. There is a noticeable difference between IGI fibers and conventional parabolic profile graded fibers, since there is no continuity in the refractive index at the core-cladding interface for the former, as shown in figure 1.
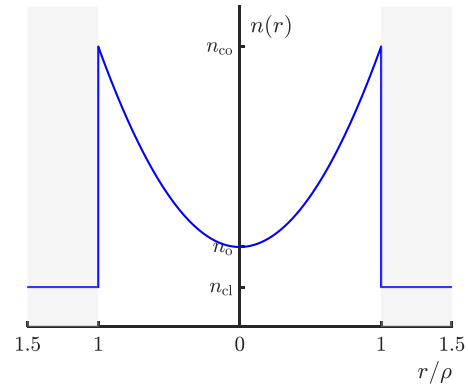

Figure 1. Refractive index profile of an IGI fiber. Radius r is normalized to the half of the fiber core diameter ($\rho = d/2$). Refer to table 1 for a more detailed description of the fiber parameters.

Table 1. Parameters of the PMMA based IGI fiber used in this work.

Parameter	Description	Value
n_{cl}	Cladding refractive index	1.402
n_{co}	Maximum core refractive index	1.492
n_o	Minimum core refractive index	1.417
Δ	Inverted profile height parameter	0.0543
d	Core diameter ($d = 2\rho$)	1 mm
θ_c	Maximum critical angle relative to the fiber axis[a]	20°

[a] Measured at the core-cladding interface.

Table 1 summarizes the main characteristics of poly-methyl methacrylate (PMMA) based fiber core that will be used throughout this work.

2.2. Ray invariants

Our starting point is the Eikonal equation [25]

$$\frac{d}{ds} \left[n(\mathbf{r}) \frac{d\mathbf{r}}{ds} \right] = \nabla n(\mathbf{r}), \quad (3)$$

where s is the distance along the ray path, and $\mathbf{r}$ represents the position vector of a point on the ray path. We can write this expression in cylindrical coordinates (r, φ, z) as follows

$$\begin{cases} \dfrac{d}{ds} \left[n(r) \dfrac{dr}{ds} \right] - rn(r) \left(\dfrac{d\varphi}{ds} \right)^2 = \dfrac{dn(r)}{dr}, \\ \dfrac{d}{ds} \left[n(r) \dfrac{d\varphi}{ds} \right] - \dfrac{2n(r)}{r} \dfrac{d\varphi}{ds} \dfrac{dr}{ds} = 0, \\ \dfrac{d}{ds} \left[n(r) \dfrac{dz}{ds} \right] = 0. \end{cases} \quad (4)$$

The third equation in equation (4) can easily be integrated, since the refractive index does not depend on the z-coordinate. Thus

$$\frac{d}{ds} \left[n(r) \frac{dz}{ds} \right] = 0 \Rightarrow n(r) \frac{dz}{ds} = \text{constant}.$$

We will call this motion constant the ray invariant $\tilde{\beta}$, and it arises from the translational invariance of the fiber. We can rewrite this expression as

$$\tilde{\beta} = n(r)\frac{\mathrm{d}z}{\mathrm{d}s} = n(r)\cos\theta_z(r), \tag{5}$$

where $\theta_z(r)$ stands for the angle between the tangent to the ray path and the axial direction z. We can use the invariant $\tilde{\beta}$ to eliminate $\mathrm{d}s$ from the first equation of equation (4) via

$$\frac{\mathrm{d}}{\mathrm{d}s} \equiv \frac{\tilde{\beta}}{n(r)}\frac{\mathrm{d}}{\mathrm{d}z} \tag{6}$$

to obtain the ray-path equation in the radial direction

$$\tilde{\beta}^2\left[\frac{\mathrm{d}^2r}{\mathrm{d}z^2} - r\left(\frac{\mathrm{d}\varphi}{\mathrm{d}z}\right)^2\right] = \frac{1}{2}\frac{\mathrm{d}n^2(r)}{\mathrm{d}r}, \tag{7}$$

whereas the azimuthal component of equation (4) will lead to a second ray invariant:

$$2\frac{\mathrm{d}r}{\mathrm{d}z}\frac{\mathrm{d}\varphi}{\mathrm{d}z} + r\frac{\mathrm{d}^2\varphi}{\mathrm{d}z^2} = 0 \Rightarrow \frac{\mathrm{d}}{\mathrm{d}z}\left(r^2\frac{\mathrm{d}\varphi}{\mathrm{d}z}\right) = 0 \Rightarrow r^2\frac{\mathrm{d}\varphi}{\mathrm{d}z} = \text{constant}.$$

This second constant is related to the azimuthal symmetry of the fiber (such an expression is reminiscent of the conservation of the angular momentum for a particle of unit mass moving under the action of a central force field [28]; notice also that it can directly be obtained from the Eikonal equation, since the refractive index does not depend on the angular coordinate). This constant is usually written in another more convenient dimensionless form that is also called the ray invariant $\tilde{l}$ [1]:

$$\tilde{l} = \tilde{\beta}\frac{r^2}{\rho}\frac{\mathrm{d}\varphi}{\mathrm{d}z}. \tag{8}$$

2.3. Ray-path equation

We will write the ray-path equation given in equation (7) in terms of the ray invariants $\tilde{\beta}$ and $\tilde{l}$. The most straightforward way is to take the square of the differential path length $\mathrm{d}s$ [29]:

$$(\mathrm{d}s)^2 = (\mathrm{d}r)^2 + r^2(\mathrm{d}\varphi)^2 + (\mathrm{d}z)^2.$$

If we divide it by $(\mathrm{d}z)^2$ and replace $\mathrm{d}s/\mathrm{d}z$ with $n(r)/\tilde{\beta}$ using equations (5) and (6), we obtain

$$\left[\frac{n(r)}{\tilde{\beta}}\right]^2 = \left(\frac{\mathrm{d}r}{\mathrm{d}z}\right)^2 + r^2\left(\frac{\mathrm{d}\varphi}{\mathrm{d}z}\right)^2 + 1.$$

Finally, if we rearrange the resultant expression and use equation (8), we have the ray-path equation

$$g(r) \equiv \tilde{\beta}^2\left(\frac{\mathrm{d}r}{\mathrm{d}z}\right)^2 = n^2(r) - \tilde{\beta}^2 - \tilde{l}^2\frac{\rho^2}{r^2}. \tag{9}$$

In the following section, we will consider specific applications of the ray-path equation (also denoted by $g(r)$).

3. Results and discussion

3.1. Classification of rays

The ray-path equation allows us to classify rays in a convenient way. Since its left-side $\tilde{\beta}^2(\mathrm{d}r/\mathrm{d}z)^2$ must necessarily be positive, ray paths can exist only if the right-side of $g(r)$ is non-negative; consequently, we will have oscillating (*propagating*) fields for the range of values of the radial coordinate r satisfying the previous condition, whereas fields will be *evanescent* for negative values of the right-side of $g(r)$.

Likewise, rays can also be classified into *meridional* and *skew* rays according to the value of the ray invariant $\tilde{l}$. If $\tilde{l} = 0$, rays will propagate in a meridional plane (i.e. a plane that contains the fiber symmetry axis), whereas if $\tilde{l} \neq 0$, rays will follow a path that excludes the fiber symmetry axis (propagation is not allowed if the last term in the right-side of $g(r)$ tends to infinity when r tends to 0).

Taking into account both considerations, we can classify rays as follows:

3.1.1. Bound rays.
These rays are bound to the fiber core, so that $g(r) < 0$ in the cladding ($\forall r > \rho$) and $g(r) > 0$ in the core ($\forall r \leqslant \rho$). At the core-cladding interface ($r = \rho$), i.e. at the turning point r_{tp}:

$$g(r)|_{r=r_{\mathrm{tp}}=\rho} = n_{\mathrm{co}}^2 - \tilde{\beta}^2 - \tilde{l}^2 > 0.$$

This condition must be fulfilled for every value of $\tilde{l}$, hence:

$$\tilde{\beta} \leqslant n_{\mathrm{co}}.$$

Furthermore, at the core-cladding interface, Snell's law dictates that the maximum value of $\theta_z(\rho)$ is:

$$\cos\theta_{z,\max}(\rho) = \cos\theta_{\mathrm{c}} = \frac{n_{\mathrm{cl}}}{n_{\mathrm{co}}}, \tag{10}$$

whereas the minimum $\tilde{\beta}$ is given by $n_{\mathrm{co}}\cos\theta_{\mathrm{c}} = n_{\mathrm{cl}}$. In summary, for bound rays:

$$\begin{cases} n_{\mathrm{cl}} \leqslant \tilde{\beta} \leqslant n_{\mathrm{co}}, \\ 0 \leqslant \tilde{l} \leqslant \tilde{l}_{\max}\left(\tilde{\beta}\right), \end{cases} \tag{11}$$

where $\tilde{l}_{\max}\left(\tilde{\beta}\right)$ is the maximum value allowed for $\tilde{l}$ in the limit $g(r) = 0$:

$$\tilde{l}_{\max}^2\left(\tilde{\beta}\right) = n_{\mathrm{co}}^2 - \tilde{\beta}^2. \tag{12}$$

We have plotted in figures 2 and 3 the ray-path equation for bound rays, considering meridional and skew rays separately. The values of the ray invariants have been chosen in order to illustrate the most representative results.

Both figures reveal that (a) ray paths only exist (non-negative values of $g(r)$) between a minimum radial coordinate denoted by r_{ic} (inner caustic radius) and the maximum ρ (except for values of the ray invariant $\tilde{\beta}$ less than n_{o}, since
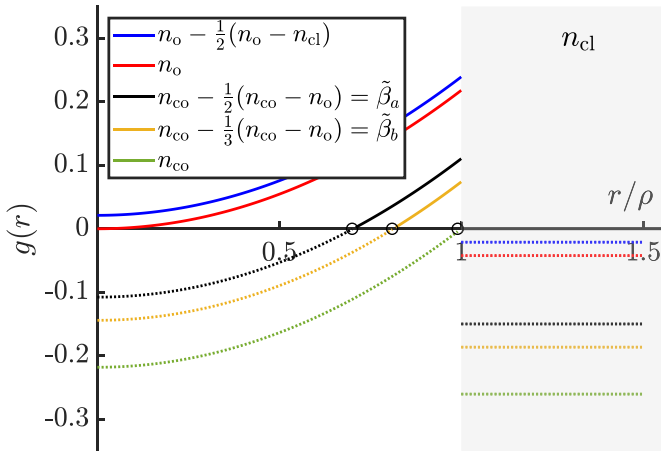
Figure 2. Ray-path equation for bound meridional rays ($\tilde{l} = 0$) as a function of fiber radius r (normalized to ρ) and for five different values of $\tilde{\beta}$ (shown in the legend). Numerical results obtained with the fiber parameters from table 1. Within the core ($r \leqslant \rho$), the non-negative values of $g(r)$ (solid lines) start from an inner caustic radius r_{ic} (the *x*-intercept point, marked by a circle) to the turning point r_{tp} in the core-cladding interface ($r_{tp} = \rho$), and they correspond to oscillating solutions. In the cladding ($r > \rho$), all values of $g(r)$ are negative (dotted lines) and lead to evanescent solutions.
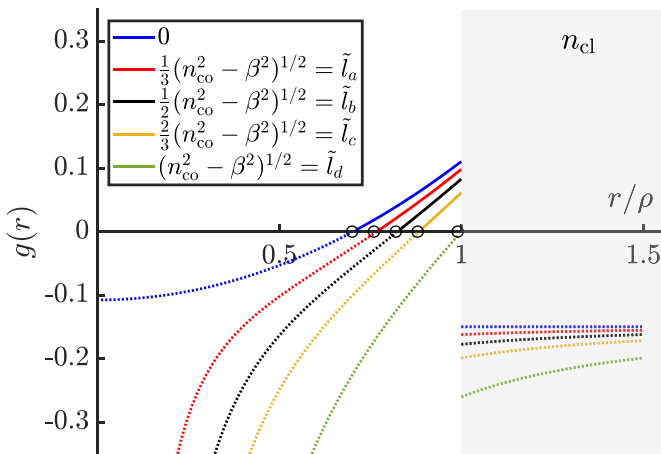

Figure 3. Ray-path equation for bound skew rays ($\tilde{l} \neq 0$) as a function of fiber radius r (normalized to ρ) and for five different values of $\tilde{l}$ (shown in the legend), with $\tilde{\beta} = n_{co} - (1/2)(n_{co} - n_o) = \tilde{\beta}_a$. For the sake of comparison, the result for bound meridional rays, $\tilde{l} = 0$, is also plotted (blue line). Each inner caustic radius r_{ic} is marked by a circle, and the turning point is again in the core-cladding interface ($r_{tp} = \rho$).

all these rays are bound meridional), and (b) ray-paths tend to concentrate in an outer ring in the vicinity of the core-cladding interface for increasing values of the ray invariants $\tilde{\beta}$ and/or $\tilde{l}$. Such a feature makes the IGI fiber interesting for sensing purposes, since the power associated to rays lies closer to the outer surface of the fiber, increasing thus the interaction of light with the surrounding medium. As will be discussed later, the values of both ray invariants will be subjected to the launching conditions (initial launching point and tilt angle relative to the fiber axis).
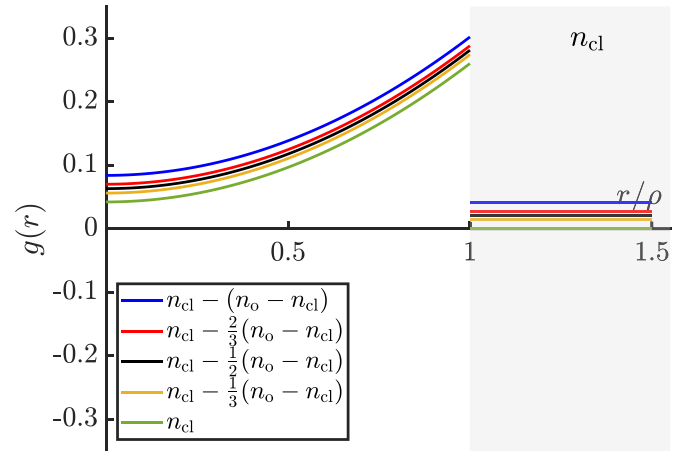

Figure 4. Ray-path equation for refracting meridional rays ($\tilde{l} = 0$) as a function of fiber radius r (normalized to ρ) and for five different values of $\tilde{\beta}$ (shown in the legend). $g(r)$ is always non-negative, so that the oscillating solutions extend across the whole core ($r \leqslant \rho$) and the cladding ($r > \rho$), and there is neither an inner caustic nor a turning point.

3.1.2. Refracting rays. These rays propagate into the cladding, so that $g(r) > 0$ in the cladding ($\forall r > \rho$). Therefore,

$$g(r) = \begin{cases} n_{cl}^2 - \tilde{\beta}^2 - \tilde{l}^2 > 0 & r = \rho, \\ n_{cl}^2 - \tilde{\beta}^2 > 0 & r \to \infty, \end{cases}$$

that is, for refracting rays:

$$0 \leqslant \tilde{\beta}^2 + \tilde{l}^2 < n_{cl}^2. \tag{13}$$

Figures 4 and 5 show the ray-path equation for refracting rays, both meridional and skew. According to figure 4, and in contrast to bound meridional rays, refracting meridional rays extend across the whole core and the cladding and there is no inner caustic. Skew refracting rays, however, extend from the inner caustic radius to the cladding (see figure 5).

In any case, since refracting rays leak power out of the fiber, launching conditions are always set in order to prevent their excitation.

3.1.3. Tunneling rays. These rays undergo a much slower leakage compared to refracting rays and satisfy simultaneously

$$\tilde{\beta} < n_{cl} \text{ and } \tilde{\beta}^2 + \tilde{l}^2 \geqslant n_{cl}^2,$$

that is, for tunneling rays:

$$\begin{cases} 0 \leqslant \tilde{\beta} < n_{cl}, \\ \left(n_{cl}^2 - \tilde{\beta}^2\right)^{1/2} \leqslant \tilde{l} \leqslant \tilde{l}_{max}\left(\tilde{\beta}\right), \end{cases} \tag{14}$$

being $\tilde{l}_{max}\left(\tilde{\beta}\right)$ the maximum value allowed for $\tilde{l}$ defined in equation (12). From the definition given in equation (14), it is clear that tunneling rays are always skew ($\tilde{l} \neq 0$).

The results shown in figure 6 suggest that tunneling rays propagating in the core *disappear* at the core-cladding
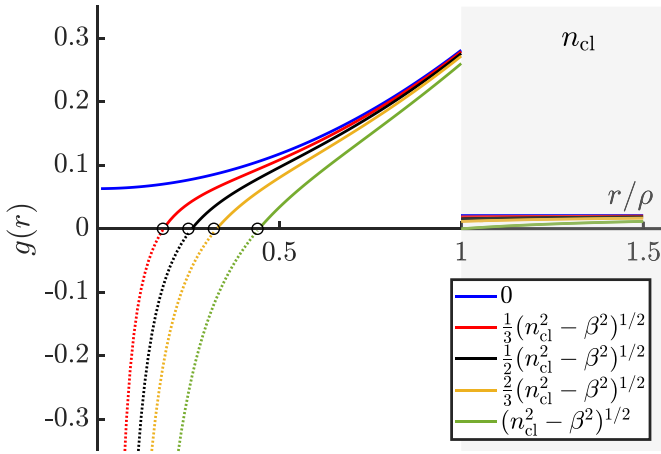
Figure 5. Ray-path equation for refracting skew rays ($\tilde{l} \neq 0$) as a function of fiber radius r (normalized to ρ) and for five different values of $\tilde{l}$ (shown in the legend), with $\tilde{\beta} = n_{\rm cl} - (1/2)(n_{\rm o} - n_{\rm cl})$. For the sake of comparison, the result for refracting meridional rays, $\tilde{l} = 0$, is also plotted (blue line). The non-negative values of $g(r)$ (solid lines), corresponding to oscillating solutions, extend from the inner caustic radius $r_{\rm ic}$ (marked by a circle) in the core ($r \leqslant \rho$) to infinity in the cladding ($r > \rho$), and there is no turning point.

interface ($r \leqslant \rho$) and *reappear* in the cladding at a finite distance (more specifically, part of the ray power is lost to the cladding by means of a tunneling mechanism due to the curvature of the core-cladding interface). This distance is referred as the radiation caustic $r_{\rm rad}$, and it can easily be obtained from $g(r)|_{r=r_{\rm rad}} = 0$:

$$r_{\rm rad} = \frac{\rho \tilde{l}}{\left(n_{\rm cl}^2 - \tilde{\beta}^2\right)^{1/2}}. \tag{15}$$

3.2. Analysis of the inner caustic radius

For a given ray path, the inner caustic is the surface defined by the radius point $r_{\rm ic}$ that makes $dr/dz|_{r=r_{\rm ic}} = 0$. As we have already pointed out, propagation of bound rays is restricted to radial components between this minimum radius and the turning point in the core-cladding interface ($r_{\rm ic} \leqslant r \leqslant \rho$).

It is straightforward to show that this inner caustic radius can be obtained from the root of the ray-path equation:

$$g(r)|_{r=r_{\rm ic}} = \tilde{\beta}^2 \left(\frac{dr}{dz}\right)^2 \bigg|_{r=r_{\rm ic}} = n^2(r_{\rm ic}) - \tilde{\beta}^2 - \tilde{l}^2 \frac{\rho^2}{r_{\rm ic}^2} = 0.$$

By substituting equation (1) into the previous equation, we solve its roots, obtaining

$$r_{\rm ic}^2 = \frac{\rho^2}{2} \left\{ \frac{\tilde{\beta}^2 - n_{\rm o}^2}{n_{\rm co}^2 - n_{\rm o}^2} \pm \left[\left(\frac{\tilde{\beta}^2 - n_{\rm o}^2}{n_{\rm co}^2 - n_{\rm o}^2}\right)^2 + \frac{4\tilde{l}^2}{n_{\rm co}^2 - n_{\rm o}^2} \right]^{1/2} \right\}, \tag{16}$$

where the minus sign must be discarded in order to satisfy the condition $r_{\rm ic}^2 \geqslant 0$ so that $r_{\rm ic}$ makes sense from a physical point
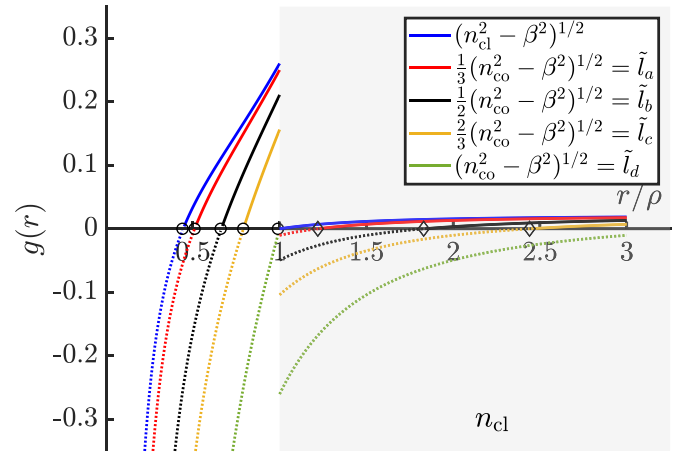

Figure 6. Ray-path equation for tunneling skew rays ($\tilde{l} \neq 0$) as a function of fiber radius r (normalized to ρ) and for five different values of $\tilde{l}$ (shown in the legend), with $\tilde{\beta} = n_{\rm co} - (1/2)(n_{\rm co} - n_{\rm o}) = \tilde{\beta}_a$. For the sake of comparison, the result for refracting skew rays, $\tilde{l} = \left(n_{\rm cl}^2 - \tilde{\beta}^2\right)^{1/2}$, is also plotted (blue line). For clarity, the x-axis is twice the original limit of figures 2–5. The non-negative values of $g(r)$ (solid lines), corresponding to oscillating solutions, extend from the inner caustic radius $r_{\rm ic}$ (marked by a circle) in the core ($r \leqslant \rho$) to the turning point $r_{\rm tp}$ in the core-cladding interface ($r_{\rm tp} = \rho$), and from the radiation caustic $r_{\rm rad}$ (marked by a diamond) in the cladding ($r > \rho$) to infinity. In between, $g(r)$ is negative (dotted lines) and, therefore, fields are evanescent (fields are said to tunnel through part of the cladding).

of view. Figure 7 allows us to analyze the results obtained from equation (16) as a function of the ray invariants $\tilde{\beta}$ and $\tilde{l}$ for bound rays.

It is remarkable that in IGI fibers, unlike in conventional fibers, inner caustics can exist even for bound meridional rays ($\tilde{l} = 0$, the magenta curve in figure 7), a favorable feature for sensing purposes. In particular, $r_{\rm ic}$ exists for meridional bound rays that satisfy the condition $n_{\rm o} \leqslant \tilde{\beta} \leqslant n_{\rm co}$, and equation (16) reduces to

$$r_{\rm ic}^2 \bigg|_{\left(\substack{n_{\rm o} \leqslant \tilde{\beta} \leqslant n_{\rm co} \\ \tilde{l}=0}\right)} = \rho^2 \left(\frac{\tilde{\beta}^2 - n_{\rm o}^2}{n_{\rm co}^2 - n_{\rm o}^2}\right), \tag{17}$$

whereas for meridional rays satisfying the condition $n_{\rm cl} \leqslant \tilde{\beta} < n_{\rm o}$, equation (16) reduces always to

$$r_{\rm ic}^2 \bigg|_{\left(\substack{n_{\rm cl} \leqslant \tilde{\beta} < n_{\rm o} \\ \tilde{l}=0}\right)} = 0. \tag{18}$$

In the latter case, instead of an inner caustic, there is an inflection point on the fiber axis ($r = 0$) because the curvature of the ray path reverses its tendency.

From a closer inspection of equation (16), we note that (a) as expected, the inner caustic radius is always $r_{\rm ic} \neq 0$ for skew rays ($\tilde{l} \neq 0$), and (b) a higher skewness increases the value of the inner caustic radius (see, for instance, the blue curve in figure 7). Both results support the fact that skew rays are more likely to convey light power closer to the core-cladding interface.
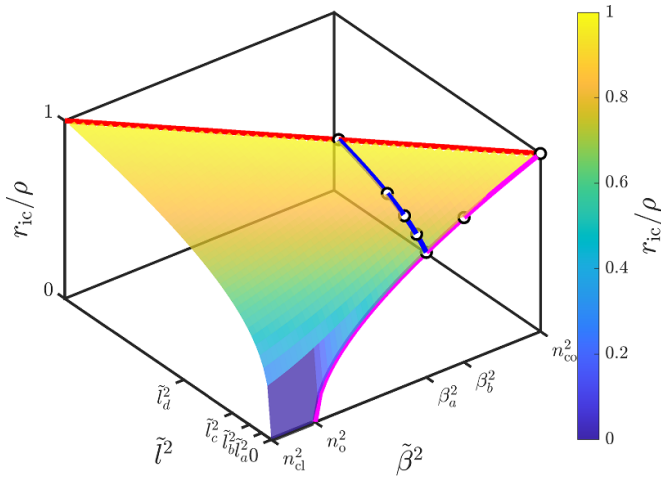
Figure 7. Normalized inner caustic radii r_{ic}/ρ as a function of the ray invariants $\tilde{\beta}$ and $\tilde{l}$ for bound rays. The red line marks the maximum limit $\tilde{\beta}^2 + \tilde{l}^2 = n_{co}^2$. The magenta curve shows the results for meridional rays ($\tilde{l} = 0$), whereas the navy curve corresponds to the results obtained for skew rays ($\tilde{l} \neq 0$) at a fixed value of $\tilde{\beta} = \tilde{\beta}_a = n_{co} - (1/2)(n_{co} - n_o)$. The inner caustics shown in figures 2 and 3 are marked again by circles: $\tilde{\beta}_a$, $\tilde{\beta}_b = n_{co} - (1/3)(n_{co} - n_o)$ and n_{co} for meridional rays ($\tilde{l} = 0$), and $\tilde{l}_a = (1/3)\left(n_{co}^2 - \tilde{\beta}_a^2\right)^{1/2}$, $\tilde{l}_b = (1/2)\left(n_{co}^2 - \tilde{\beta}_a^2\right)^{1/2}$, $\tilde{l}_c = (2/3)\left(n_{co}^2 - \tilde{\beta}_a^2\right)^{1/2}$, and $\tilde{l}_d = \left(n_{co}^2 - \tilde{\beta}_a^2\right)^{1/2}$ for skew rays ($\tilde{l} \neq 0$) at $\tilde{\beta} = \tilde{\beta}_a$, respectively.

Consequently, and keeping in mind the use of IGI fibers in sensing applications, it will be crucial to set the appropriate launching conditions to ensure the excitation of either meridional bound rays with sufficiently high values of the ray invariant $\tilde{\beta}$ and/or skew rays with a certain degree of skewness.

3.3. Effects of launching conditions on ray-paths

For simplicity, we will restrict the analysis of launching conditions to bound rays only; in addition, we will address their effects on meridional and skew rays separately. We will assume an incoming ray at the entrance point r_0 and tilted at an angle θ_0 to the fiber axis (this tilt angle is defined inside the core, so that $\theta_z(r_0) = \theta_0$). The condition for a ray to be bound has been stated in equation (11). Therefore, we have

$$\tilde{\beta} \geqslant n_{cl} \Rightarrow n(r_0)\cos\theta_0 \geqslant n_{cl}.$$

If we substitute equation (1) into the left-side

$$n_o\left[1 + 2\Delta\left(\frac{r_0}{\rho}\right)^2\right]^{1/2}\cos\theta_0 \geqslant n_{cl},$$

we can find the maximum tilt angle allowed for a bound ray launched at r_0:

$$\theta_0|_{max} \leqslant \arccos\left\{\frac{n_{cl}}{n_o}\left[1 + 2\Delta\left(\frac{r_0}{\rho}\right)^2\right]^{-1/2}\right\}. \tag{19}$$

3.3.1. Meridional rays.
As pointed out previously, depending on the condition satisfied by the current value of the ray invariant $\tilde{\beta}$, the ray path will have either an inner caustic ($r_{ic} \neq 0$, the ray will never reach the fiber axis) or an inflection point on the fiber axis ($r_{ic} = 0$); refer also to equations (17) and (18). Consequently, $\tilde{\beta} = n_o$ sets the limit that separates both conditions. From this limit, we will calculate the launching conditions that lead either to an inner caustic or to an inflection point:

$$\tilde{\beta} = n_o \Rightarrow n(r_0)\cos\theta_0 = n_o.$$

If we substitute equation (1) into the left-side and square both sides, we have

$$n_o^2\left[1 + 2\Delta\left(\frac{r_0}{\rho}\right)^2\right]\cos^2\theta_0 = n_o^2.$$

Finally, after some rearrangement:

$$r_0^2\left(\frac{\sqrt{2\Delta}}{\rho}\right)^2 = \tan^2\theta_0.$$

In summary, we have:

$$\begin{cases} \text{inner caustic} & \text{if } |\tan\theta_0| \leqslant r_0\left(\sqrt{2\Delta}/\rho\right), \\ \text{inflection point} & \text{if } |\tan\theta_0| > r_0\left(\sqrt{2\Delta}/\rho\right). \end{cases} \tag{20}$$

Next, we will show the general shape of the ray paths of bound meridional rays through an IGI fiber. Without loss of generality, we will now assume that the rays launched at the input surface of the fiber are within the xz-plane, since all the planes containing the fiber symmetry axis are equivalent (the refractive index is axisymmetric). Under such circumstances, it is more convenient to write the Eikonal equation given in equation (3) in Cartesian coordinates (x, y, z). After some rearrangement, it is straightforward to show that, on the one hand, the ray-path equation defined in equation (7) reduces to

$$\begin{cases} \tilde{\beta}^2\left(\dfrac{d^2x}{dz^2}\right) = \dfrac{1}{2}\dfrac{dn^2(x,y)}{dx}, \\ \tilde{\beta}^2\left(\dfrac{d^2y}{dz^2}\right) = \dfrac{1}{2}\dfrac{dn^2(x,y)}{dy}, \end{cases} \tag{21}$$

and, on the other, the refractive index of equation (1) is written as

$$n^2(x,y) = \begin{cases} n_o^2\left[1 + 2\Delta\left(\frac{x^2+y^2}{\rho^2}\right)\right] & x^2 + y^2 \leqslant \rho^2, \\ n_{cl}^2 & x^2 + y^2 > \rho^2. \end{cases} \tag{22}$$

Both expressions are further reduced within the xz-plane, since $y = 0$, and, therefore, we only have to solve:

$$\tilde{\beta}^2\left(\frac{d^2x}{dz^2}\right) = \frac{1}{2}\frac{d\left[n_o^2\left(1 + 2\Delta\frac{x^2}{\rho^2}\right)\right]}{dx} = \frac{n_o^2 2\Delta}{\rho^2}x.$$
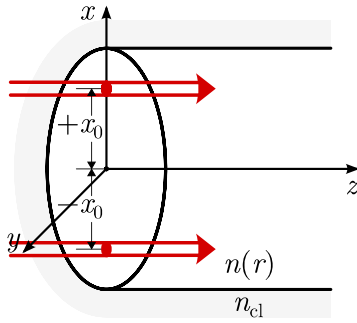
Figure 8. Launching conditions of meridional rays parallel to the fiber axis and contained in the *xz*-plane. $\pm x_0$ stands for the initial launching point.

This expression leads to

$$\frac{\mathrm{d}^2 x}{\mathrm{d}z^2} = \frac{n_o^2 2\Delta}{\tilde{\beta}^2 \rho^2} x,$$

whose solution is

$$x(z) = A \sinh(\Gamma z) + B \cosh(\Gamma z), \tag{23}$$

where

$$\Gamma^2 = \frac{n_o^2 2\Delta}{\tilde{\beta}^2 \rho^2}, \tag{24}$$

being *A* and *B* two length constants to be determined from the launching conditions $x_0 = r_0$ and θ_0. Here, the ray invariant $\tilde{\beta}$ from equation (5) is evaluated as

$$\tilde{\beta} = n(x,0)\cos\theta_z(x,0) = n(x_0,0)\cos\theta_0.$$

3.3.1.1. Meridional rays parallel to the fiber axis. Let us now consider the case of light beams injected into the fiber parallel to the fiber axis ($\theta_0 = 0$) from the initial entrance point $\pm x_0$, as shown in figure 8.

We determine the length constants *A* and *B* of equation (23) by invoking at the input of the fiber ($z = 0$):

$$\begin{cases} x(0) = x_0 & \Rightarrow & A\sinh(\Gamma 0) + B\cosh(\Gamma 0) = x_0, \\ \frac{\mathrm{d}x(z)}{\mathrm{d}z}\Big|_{z=0} = \tan\theta_0 = 0 & \Rightarrow & A\Gamma\cosh(\Gamma 0) + B\Gamma\sinh(\Gamma 0) = 0. \end{cases}$$

Then, we obtain $A = 0$ and $B = x_0$. Consequently,

$$x(z) = x_0 \cosh(\Gamma z). \tag{25}$$

It is straightforward to calculate the *z*-coordinates of the first inner caustic and the first turning point. For the former, we must set $[\mathrm{d}x(z)/\mathrm{d}z]|_{z=z_{ic,1}} = 0$, so that $z_{ic,1} = 0$. For the latter, we have $\pm x(z_{tp,1}) = \pm\rho$. Hence,

$$z_{tp,1} = \frac{1}{\Gamma} \mathrm{arccosh}\left(\frac{\rho}{x_0}\right), \tag{26}$$
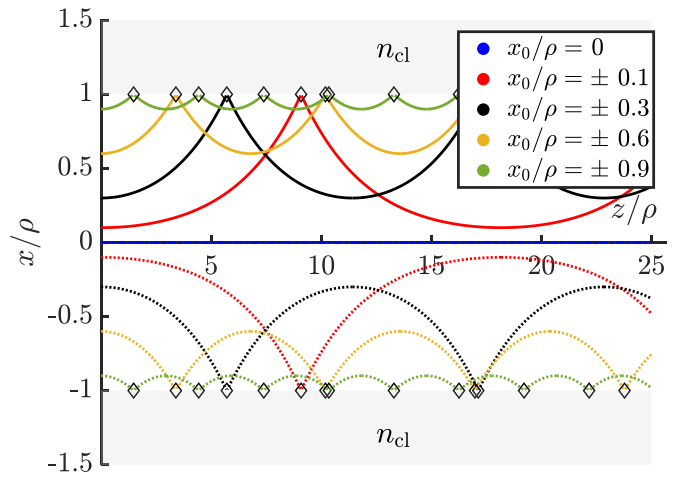

Figure 9. Geometric paths described by bound meridional rays launched parallel to the fiber axis and contained in the *xz*-plane. Results obtained for different $\pm x_0$ initial launching points (shown in the legend): solid lines for positive launching points ($+x_0$) and dotted lines for negative ones ($-x_0$). Each ray undergoes total internal reflection whenever it reaches the turning point at the core-cladding interface (marked by a diamond). Ray-paths are closest to the center at the inner caustics. There are no inflection points for meridional rays launched parallel to the fiber axis. Rays launched in the center of the fiber, $x_0 = 0$ (dash-dotted blue line), always propagate along the center (they have neither inner caustics nor inflection points).

and the ray half-period z_p, defined as the axial distance between successive turning points, is then calculated as

$$z_p = \frac{2}{\Gamma} \mathrm{arccosh}\left(\frac{\rho}{x_0}\right), \tag{27}$$

since $z_p = 2|z_{tp,1} - z_{ic,1}|$.

Figure 9 shows the ray paths obtained using equation (25) for different values of the initial launching point $\pm x_0$ (notice that the results shown in the figures hereafter are only intended for a better understanding of the ray trajectories obtained from the analytical expressions). It can be observed that there are no inflection points for meridional rays launched parallel to the fiber axis: indeed, in equation (20) we have $x_0\left(\sqrt{2\Delta}/\rho\right) \geqslant 0$, i.e. there are only inner caustics (notice that rays launched in the center of the fiber, $x_0 = 0$, propagate only along the fiber axis and have neither inflection points nor inner caustics). In addition, at each inner caustic z_{ic}, the closest position to the center coincides with the corresponding initial launching point x_0.

At each turning point z_{tp}, a ray undergoes total internal reflection and its axial angle is at its highest value (θ_{tp}, see appendix A), which is always below the maximum tilt angle allowed for a bound ray given by equation (19). From these observations, it can be concluded that, if collimated light is impinged on the input surface of the fiber, the initial launching point should lie as close as possible to the core-cladding interface in order to confine light power to the outermost part of the core.
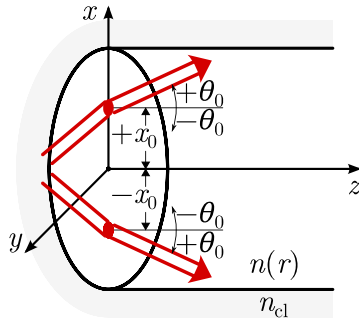
Figure 10. Launching conditions of meridional rays tilted at an angle θ_0 to the fiber axis and contained in the xz-plane. $\pm x_0$ stands for the initial launching point and θ_0 takes positive or negative values according to the convention shown in the figure.

3.3.1.2. Meridional rays tilted to the fiber axis.   In this case, light beams are injected into the fiber tilted at an angle θ_0 to the fiber axis from the initial entrance point $\pm x_0$, as shown in figure 10.

The length constants A and B of equation (23) are now set by invoking at the input of the fiber ($z = 0$):

$$\begin{cases} x(0) = x_0 & \Rightarrow \quad A\sinh(\Gamma 0) + B\cosh(\Gamma 0) = x_0, \\ \left.\dfrac{dx(z)}{dz}\right|_{z=0} = \tan\theta_0 & \Rightarrow \quad A\Gamma\cosh(\Gamma 0) + B\Gamma\sinh(\Gamma 0) = \tan\theta_0, \end{cases}$$

so that $A = \tan\theta_0/\Gamma$ and $B = x_0$. Thus,

$$x(z) = \frac{\tan\theta_0}{\Gamma}\sinh(\Gamma z) + x_0\cosh(\Gamma z). \tag{28}$$

Figures 11 and 12 show the ray paths obtained using equation (28) for different values of the initial tilt angle $\pm\theta_0$ and the initial launching point $\pm x_0$.

Unlike in the preceding case, depending on the initial launching conditions, rays will either go through the center of the fiber, with a change of sign in the curvature of their trajectory (in other words, there are inflection points), or they will never reach the center of the fiber (i.e. there are inner caustics). Again, equation (20) dictates whether we have an inner caustic or an inflection point (notice that $r_0 = |x_0|$ in equation (20)). The results plotted in both figures allow us to complete the whole picture of ray paths as a function of launching conditions: for sensing purposes, and in order to ensure the confinement of light power in the outermost part of the fiber core, it is necessary to impinge light on the input surface of the fiber not only closest to the core-cladding interface but also with a tilt angle as small as possible.

Let us now calculate the z-coordinate of the first inner caustic or the first inflection point from the ray path obtained using equation (28).

(a) For the first inner caustic $z_{ic,1}$, we must set $\left.\left[dx(z)/dz\right]\right|_{z=z_{ic,1}} = 0$. Therefore,

$$z_{ic,1} = \frac{1}{\Gamma}\operatorname{arctanh}\left(\frac{-\tan\theta_0}{x_0\Gamma}\right), \tag{29}$$

valid if $|\tan\theta_0| < |x_0|\Gamma$ and $x_0 \neq 0$. It turns out that both conditions are automatically fulfilled when $|\tan\theta_0| \leqslant |x_0|\left(\sqrt{2\Delta}/\rho\right)$ (refer back to equation (20)).

(b) For the first inflection point $z_{ip,1}$, we must set $\left.\left[d^2x(z)/dz^2\right]\right|_{z=z_{ip,1}} = 0$ (notice that $\left[d^2x(z)/dz^2\right] = \Gamma^2 x(z)$, which is an expected result for an oscillating solution satisfying the ray equation). Consequently,

$$z_{ip,1} = \frac{1}{\Gamma}\operatorname{arctanh}\left(\frac{-x_0\Gamma}{\tan\theta_0}\right), \tag{30}$$

valid if $|\tan\theta_0| > |x_0|\Gamma$, which is automatically fulfilled when $|\tan\theta_0| > |x_0|\left(\sqrt{2\Delta}/\rho\right)$ (see again equation (20)).

As to the z-coordinate of the first turning point, now we have to set $|x(z_{tp,1})| = \rho$. More specifically:

$$\begin{cases} \text{if } x_0 \geqslant 0 & x(z_{tp,1}) \\ & = \begin{cases} -\rho & \text{if } |\tan\theta_0| > |x_0|\Gamma \text{ and } \tan\theta_0 < 0, \\ +\rho & \text{rest of cases,} \end{cases} \\ \text{if } x_0 < 0 & x(z_{tp,1}) \\ & = \begin{cases} +\rho & \text{if } |\tan\theta_0| > |x_0|\Gamma \text{ and } \tan\theta_0 > 0, \\ -\rho & \text{rest of cases.} \end{cases} \end{cases} \tag{31}$$

By solving the equation above (see appendix B for details), we determine

$$\begin{cases} \text{if } x_0 \geqslant 0 & z_{tp,1} \\ & = \begin{cases} \frac{1}{\Gamma}\operatorname{arccosh}(-F) & \text{if } |\tan\theta_0| > |x_0|\Gamma \text{ and} \\ & \qquad\qquad \tan\theta_0 < 0, \\ \frac{1}{\Gamma}\operatorname{arccosh}(+F) & \text{rest of cases,} \end{cases} \\ \text{if } x_0 < 0 & z_{tp,1} \\ & = \begin{cases} \frac{1}{\Gamma}\operatorname{arccosh}(+F) & \text{if } |\tan\theta_0| > |x_0|\Gamma \text{ and} \\ & \qquad\qquad \tan\theta_0 > 0, \\ \frac{1}{\Gamma}\operatorname{arccosh}(-F) & \text{rest of cases,} \end{cases} \end{cases} \tag{32}$$

where

$$F = \frac{-\rho x_0\Gamma^2 + \tan\theta_0\left[\tan^2\theta_0 + \Gamma^2\left(\rho^2 - x_0^2\right)\right]^{1/2}}{\tan^2\theta_0 - x_0^2\Gamma^2}.$$

Finally, the ray half-period z_p is calculated in accordance with equation (20) as

$$z_p = \begin{cases} 2\left(z_{tp,1} - z_{ic,1}\right) & \text{if } |\tan\theta_0| \leqslant |x_0|\left(\sqrt{2\Delta}/\rho\right), \\ 2\left(z_{tp,1} - z_{ip,1}\right) & \text{if } |\tan\theta_0| > |x_0|\left(\sqrt{2\Delta}/\rho\right), \end{cases} \tag{33}$$

where $z_{ic,1}$ and $z_{ip,1}$ are given by equations (29) and (30), respectively.

3.3.2 Skew rays.   We can make use of equations (21) and (22) to show the general shape of the ray paths of bound skew rays projected to a plane perpendicular to the axial direction z. It is straightforward to show that the ray-path equation is now expressible in the following form
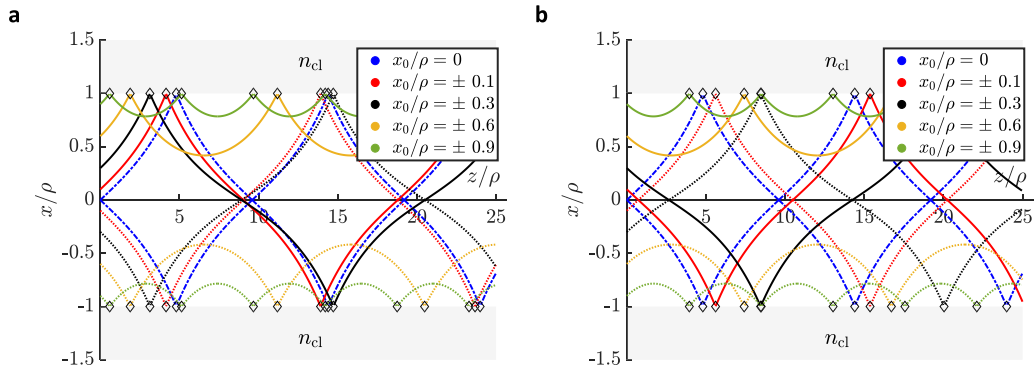
Figure 11. Geometric paths described by bound meridional rays launched tilted to the fiber axis and contained in the *xz*-plane. Results obtained for (a) $\theta_0 = +8°$ and (b) $\theta_0 = -8°$, and for different $\pm x_0$ initial launching points (shown in the legend): solid lines for positive launching points $(+x_0)$ and dotted lines for negative ones $(-x_0)$. The absolute value of θ_0 is always less than the most restrictive maximum axial angle for bound rays (equation (19) for $\min r_0 = \min |x_0|$, which corresponds to rays launched at $x_0 = 0$, i.e. $\left| \theta_0 \right|_{\max, x_0 = 0} = 8.34°$). Each ray undergoes total internal reflection whenever it reaches the turning point at the core-cladding interface (marked by a diamond). Ray-paths reveal inner caustics for launching points $x_0/\rho = \pm 0.6$ and ± 0.9, whereas for lower launching points in absolute value there are inflections points, in accordance with the condition of equation (20). Rays launched in the center of the fiber, $x_0 = 0$ (dash-dotted blue lines, corresponding to $\theta_0 = +8°$ and $-8°$ both in (a) and (b)), have only inflection points.
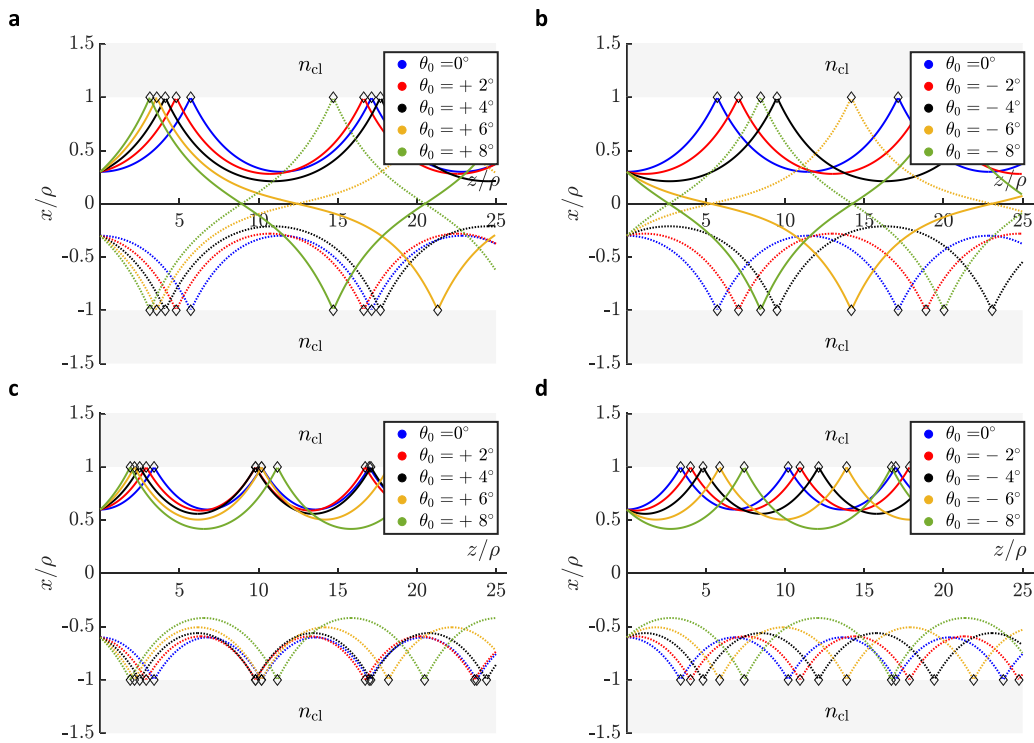

Figure 12. Geometric paths described by bound meridional rays launched tilted to the fiber axis and contained in the *xz*-plane. Results obtained for $x_0/\rho = \pm 0.3$ and ± 0.6, and for different initial tilt angles θ_0 (shown in the legend): solid lines for positive launching points $(+x_0)$ and dotted lines for negative ones $(-x_0)$. (a) $x_0/\rho = \pm 0.3$ and $\theta_0 \geqslant 0$; (b) $x_0/\rho = \pm 0.3$ and $\theta_0 \leqslant 0$; (c) $x_0/\rho = \pm 0.6$ and $\theta_0 \geqslant 0$; (d) $x_0/\rho = \pm 0.6$ and $\theta_0 \leqslant 0$. The maximum absolute value of θ_0 (8°) is always less than the most restrictive maximum axial angle for bound rays (equation (19) for $\min r_0 = \min |x_0|$, which corresponds to rays launched at $x_0/\rho = \pm 0.3$, i.e. $\left| \theta_0 \right|_{\max, |x_0/\rho| = 0.3} = 10.06°$). Each ray undergoes total internal reflection whenever it reaches the turning point at the core-cladding interface (marked by a diamond). Ray-paths reveal only inner caustics for launching points $x_0 = \pm 0.6$ irrespective of θ_0, whereas there are inflection points for launching points $x_0 = \pm 0.3$ provided that θ_0 is sufficiently high to satisfy the condition $|\tan \theta_0| > |x_0| \left(\sqrt{2\Delta}/\rho \right)$.

$$\begin{cases} \tilde{\beta}^2 \left(\frac{\mathrm{d}^2 x}{\mathrm{d}z^2} \right) = \frac{n_\mathrm{o}^2 2\Delta}{\rho^2} x \Rightarrow \frac{\mathrm{d}^2 x}{\mathrm{d}z^2} = \Gamma^2 x, \\ \tilde{\beta}^2 \left(\frac{\mathrm{d}^2 y}{\mathrm{d}z^2} \right) = \frac{n_\mathrm{o}^2 2\Delta}{\rho^2} y \Rightarrow \frac{\mathrm{d}^2 y}{\mathrm{d}z^2} = \Gamma^2 y, \end{cases}$$

where Γ has been defined in equation (24).

Therefore, by solving the previous set of independent differential equations, we obtain

$$\begin{cases} x(z) = A \sinh(\Gamma z) + B \cosh(\Gamma z), \\ y(z) = C \sinh(\Gamma z) + D \cosh(\Gamma z), \end{cases} \quad (34)$$

and, again, A, B, C, and D are length constants to be determined from the launching conditions $\left(x_0^2 + y_0^2 \right)^{1/2} = r_0$ and θ_0.

Let us consider light beams injected into the fiber tilted at an angle θ_0 to the fiber axis on a non-meridional-plane from the initial entrance point r_0; for simplicity, we will set this entrance point within the xz-plane, so that $x_0 = r_0$ and $y_0 = 0$, and the tilt angle θ_0 will be formed within the yz-plane. The length constants A, B, C, and D of equation (34) are now obtained by setting at the input of the fiber ($z = 0$):

$$\begin{cases} x(0) = x_0 & \Rightarrow & A \sinh(\Gamma 0) + B \cosh(\Gamma 0) = x_0, \\ \frac{\mathrm{d}x(z)}{\mathrm{d}z} \Big|_{z=0} = 0 & \Rightarrow & A\Gamma \cosh(\Gamma 0) + B\Gamma \sinh(\Gamma 0) = 0, \\ y(0) = 0 & \Rightarrow & C \sinh(\Gamma 0) + D \cosh(\Gamma 0) = 0, \\ \frac{\mathrm{d}y(z)}{\mathrm{d}z} \Big|_{z=0} = \tan\theta_0 & \Rightarrow & C\Gamma \cosh(\Gamma 0) + D\Gamma \sinh(\Gamma 0) = \tan\theta_0, \end{cases}$$

so that $A = 0$, $B = x_0$, $C = \tan\theta_0/\Gamma$ and $D = 0$. Thus,

$$\begin{cases} x(z) = x_0 \cosh(\Gamma z), \\ y(z) = \frac{\tan\theta_0}{\Gamma} \sinh(\Gamma z), \end{cases} \quad (35)$$

and, therefore, we obtain a set of parametric equations that correspond to a hyperbola (indeed, if we sum the squares of both equations and apply hyperbolic identities, we have the equation of a hyperbola $x^2/x_0^2 - y^2/(\tan\theta_0/\Gamma)^2 = 1$; likewise, if the condition $|x_0| = \left(\rho/\sqrt{2\Delta} \right) |\tan\theta_0|$ is also satisfied, this hyperbola becomes rectangular). Additionally, it can also be proven that the z-coordinate of the first turning point is given by the following compact analytical expression

$$z_{\mathrm{tp},1} = \frac{1}{\Gamma} \mathrm{arccosh} \left[\frac{\rho^2 + (\tan\theta_0/\Gamma)^2}{x_0^2 + (\tan\theta_0/\Gamma)^2} \right]^{1/2}, \quad (36)$$

whereas the z-coordinate of the first inner caustic is always $z_{\mathrm{ic},1} = 0$ because, under such launching conditions, each inner caustic coincides with the initial launching point x_0. Thus, the ray half-period z_p is

$$z_\mathrm{p} = \frac{2}{\Gamma} \mathrm{arccosh} \left[\frac{\rho^2 + (\tan\theta_0/\Gamma)^2}{x_0^2 + (\tan\theta_0/\Gamma)^2} \right]^{1/2}. \quad (37)$$

(Notice that, if $\theta_0 = 0$ is satisfied, both expressions reduce to equations (26) and (27), respectively, since then we would be dealing with meridional rays launched parallel to the fiber axis.)

Using equation (35), we have plotted in figure 13 the projection of the evolution of the ray paths in a plane perpendicular to

the axial direction z for different values of the initial tilt angle $+\theta_0$ and the initial launching point $+x_0$, starting from $N_{\mathrm{tp}} = 2$ turning points to $N_{\mathrm{tp}} = 16$. Notice that negative values of the initial tilt angle, $-\theta_0$, imply that rays start evolving counterclockwise (instead of clockwise); we have also omitted the results obtained for negative values of the initial launching point, $-x_0$, because they do not make any significant contribution to the discussion. Furthermore, and as expected for a meridional ray, when $\theta_0 = 0$ the projection is a straight line.

According to the results, it is clear that each inner caustic coincides with the initial launching point x_0 and it has nothing to do with the tilt angle θ_0 as long as this angle is measured in the yz-plane. Increasing the tilt angle θ_0, the projections of ray paths in the xy-plane describe longer arc lengths and successive turning points are more spaced, whereas the ray half-period z_p is shortened according to equation (37), so that the ray travels a longer path inside the fiber. By launching rays closer to the core-cladding interface, not only does the light power confine in the outermost part of the fiber, but the ray half-period z_p is further reduced, increasing the exposure of light rays to the core-cladding interface per unit length, a fact that could be advantageous for sensing purposes.

We conclude this section by taking the more general launching conditions $\left(x_0^2 + y_0^2 \right)^{1/2} = r_0$ and θ_0 without any of the constraints shown above. It turns out that the ray half-period z_p is more conveniently calculated from the ray-path equation given in equation (9) as a function of the ray invariants $\tilde{\beta}$ and $\tilde{l}$. The ray path $z(r)$ can be calculated as

$$\frac{\mathrm{d}r}{\mathrm{d}z} = \left[\frac{g(r)}{\tilde{\beta}^2} \right]^{1/2} \Rightarrow z(r) = z_0 + \tilde{\beta} \int_{r_0}^{r} \frac{\mathrm{d}r'}{[g(r')]^{1/2}}$$

$$= z_0 + \tilde{\beta} \int_{r_0}^{r} \left[n^2(r') - \tilde{\beta}^2 - \tilde{l}^2 \frac{\rho^2}{(r')^2} \right]^{-1/2} \mathrm{d}r'. \quad (38)$$

This integral can be solved analytically (see appendix C for details), yielding

$$z(r) = z_0 + \frac{1}{2\Gamma} \mathrm{arccosh} \left[\frac{(r')^2 - \alpha^2}{\gamma} \right] \Big|_{r_0}^{r}, \quad (39)$$

where Γ has already been defined in equation (24), the parameters α and γ are

$$\alpha^2 = \left(\tilde{\beta}^2 - n_\mathrm{o}^2 \right) \frac{\rho^2/2}{n_\mathrm{o}^2 2\Delta} \text{ and } \gamma = \left(\tilde{l}^2 \frac{\rho^4}{n_\mathrm{o}^2 2\Delta} + \alpha^4 \right)^{1/2}, \quad (40)$$

and the ray invariant $\tilde{l}$ is obtained from equation (8).

Therefore, the ray half-period z_p is finally calculated as (refer again to appendix C for further details)

$$z_\mathrm{p} = \frac{1}{\Gamma} \left| \mathrm{arccosh} \left(\frac{\rho^2 - \alpha^2}{\gamma} \right) - \mathrm{arccosh} \left(\frac{r_\mathrm{ic}^2 - \alpha^2}{\gamma} \right) \right|, \quad (41)$$

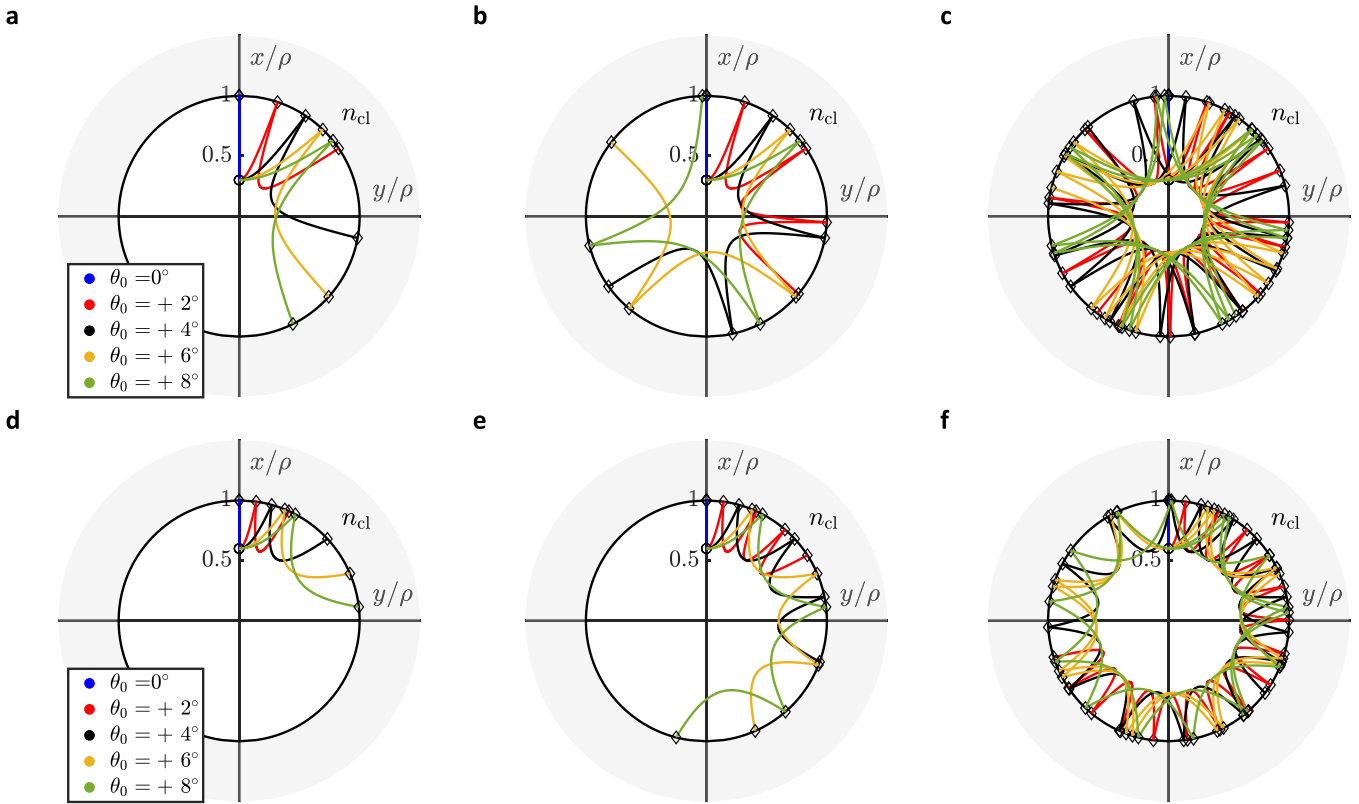being r_ic given in equation (16).

Figure 13. Transverse projection to the fiber cross-section of the geometric paths described by skew rays launched tilted to the fiber axis. Results obtained for $x_0/\rho = +0.3$ (upper panels: (a)–(c)) and $+0.6$ (lower panels: (d)–(f)), and for different initial tilt angles θ_0 measured in the yz-plane (refer to both legends), showing the evolution of ray-paths from $N_{tp} = 2$ turning points (left-hand panels: (a), (d)), through $N_{tp} = 4$ (central panels: (b), (e)), to $N_{tp} = 16$ (right-hand panels: (c), (f)). For the sake of comparison, the results of $\theta_0 = 0$, which correspond to meridional rays, are also plotted (blue lines). Each ray undergoes total internal reflection whenever it reaches the turning point at the core-cladding interface (marked by a diamond). Ray-paths reveal only inner caustics (there are no inflection points for skew rays, since, by definition, they never reach the center of the fiber) and each inner caustic coincides with the corresponding initial launching point x_0 regardless of the value of the tilt angle θ_0.

It is possible to test the validity of equation (41) by computing numerically the ray half-period z_p for the launching conditions we have considered above for skew rays (initial entrance point r_0 within the xz-plane, $x_0 = r_0$, $y_0 = 0$, and tilt angle θ_0 formed within the yz-plane) and by comparing it with the result of equation (37). For this purpose, it is necessary to obtain the ray invariants $\tilde{\beta}$ and $\tilde{l}$ using equations (5) and (8), respectively. On the one hand, the ray invariant $\tilde{\beta}$ is straightforwardly calculated by taking $n(r) = n(x_0, 0)$ using equation (22) and $\theta_z(r) = \theta_0$, so that

$$\tilde{\beta} = n(x_0, 0)\cos\theta_0.$$

On the other hand, the ray invariant $\tilde{l}$ requires calculating $d\varphi/dz$ at the input of the fiber ($z = 0$). Taking into account that $\varphi(z) = \arctan[y(z)/x(z)]$, and substituting equation (35) into the latter, we obtain

$$\frac{d\varphi}{dz} = \frac{(\tan\theta_0)/x_0}{1 + \{[(\tan\theta_0)/(x_0\Gamma)]\tanh(\Gamma z)\}^2}\cosh^2(\Gamma z),$$

so that at the input of the fiber ($z = 0$) we have $(d\varphi/dz)|_{z=0} = (\tan\theta_0)/x_0$, leading to

$$\tilde{l} = \tilde{\beta}(x_0/\rho)\tan\theta_0 = n(x_0, 0)(x_0/\rho)\sin\theta_0.$$

The parameters α and γ are then obtained from the substitution of both ray invariants $\tilde{\beta}$ and $\tilde{l}$ into equation (40). It turns out that $\gamma = x_0^2 - \alpha^2$; consequently, and taking into account that $r_{ic} = x_0$, the second inverse hyperbolic cosine of equation (41) equals zero and, therefore, the ray half-period z_p reduces to

$$z_p = \frac{1}{\Gamma}\text{arccosh}\left(\frac{\rho^2 - \alpha^2}{\gamma}\right),$$

leading to the same numerical results obtained from equation (37).

4. Conclusions

In this work, we have analyzed the light propagation properties of multimode optical fibers with inverted refractive index profiles by using the classical geometric optics approach. We have derived the ray-path equation and the ray invariants that allow us both to classify rays into bound, refracting and tunneling, and to calculate the ray trajectories inside IGI fibers.

We have analyzed the behavior of these fibers under different launching conditions and proved that the inverted refractive index profile of these fibers favors the propagation of light

power closer to the core-cladding interface, provided that ray invariants are sufficiently high or, at least, rays exhibit a certain degree of skewness. We have also showed and concluded that launching collimated light closer to the core-cladding interface ensures a better confinement of light power in the outermost part of the core, a fact that could be exploited for sensing, solar and light amplification purposes.

Data availability statement

The data that support the findings of this study are available upon reasonable request from the authors.

Acknowledgments

Conflict of interest

The authors declare that they have no affiliations with or involvement in any organization or entity with any financial interest in the subject matter or materials discussed in this manuscript.

Appendix A. Highest axial angle of a meridional bound ray launched parallel to the fiber axis

We can calculate at any turning point z_{tp} the highest axial angle θ_{tp} of a meridional bound ray launched parallel to the fiber axis in the following two ways:

(a) From the slope of the ray path: $\tan\theta_{tp} = (dx/dz)|_{z=z_{tp}}$. Thus, taking the derivative of equation (25) and substituting equation (26) into this derivative, we have

$$\tan\theta_{tp} = \left.\frac{dx}{dz}\right|_{z=z_{tp,1}} = x_0\Gamma\sinh\left[\operatorname{arccosh}\left(\frac{\rho}{x_0}\right)\right].$$

By applying hyperbolic identities:

$$\tan\theta_{tp} = x_0\Gamma\left\{\cosh^2\left[\operatorname{arccosh}\left(\frac{\rho}{x_0}\right)\right] - 1\right\}^{1/2}$$
$$= x_0\Gamma\left[\left(\frac{\rho}{x_0}\right)^2 - 1\right]^{1/2}.$$

Therefore:

$$\theta_{tp} = \arctan\left[\Gamma\left(\rho^2 - x_0^2\right)^{1/2}\right]. \qquad (A1)$$

(b) From the ray invariant $\tilde{\beta}$: $\cos\theta_{tp} = \cos\theta_z(\rho, 0) = \tilde{\beta}/n(\rho, 0)$. For convenience, we apply trigonometric identities, obtaining

$$\tan\theta_{tp} = \frac{\left(n^2(\rho, 0) - \tilde{\beta}^2\right)^{1/2}}{\tilde{\beta}} = \frac{\left(n_{co}^2 - \tilde{\beta}^2\right)^{1/2}}{\tilde{\beta}}.$$

Since we have $\tilde{\beta} = n(x_0, 0)\cos 0$ at the input surface of the fiber, we can write

$$\tan\theta_{tp} = \frac{\left(n_{co}^2 - n^2(x_0, 0)\right)^{1/2}}{\tilde{\beta}} = \frac{\left[n_{co}^2 - n_o^2\left(1 + 2\Delta\frac{x_0^2}{\rho^2}\right)\right]^{1/2}}{\tilde{\beta}}$$
$$= \frac{n_o\sqrt{2\Delta}}{\tilde{\beta}\rho}\left(\rho^2 - x_0^2\right)^{1/2},$$

so that, taking into account equation (24), we obtain again the same analytical expression given by equation (A1).

Appendix B. Longitudinal coordinate of the first turning point of a bound meridional ray launched tilted to the axial angle

In order to obtain the *z*-coordinate of the first turning point, we can proceed by solving $x(z_{tp,1}) = s\rho$, where *s* is $+1$ or -1 according to the conditions stated in equation (31), i.e.

$$\begin{cases} \text{if } x_0 \geqslant 0 & s = \begin{cases} -1 & \text{if } |\tan\theta_0| > |x_0|\Gamma \text{ and } \tan\theta_0 < 0, \\ +1 & \text{rest of cases}, \end{cases} \\ \text{if } x_0 < 0 & s = \begin{cases} +1 & \text{if } |\tan\theta_0| > |x_0|\Gamma \text{ and } \tan\theta_0 > 0, \\ -1 & \text{rest of cases}. \end{cases} \end{cases}$$
$$(B1)$$

Thus, by substituting equation (28),

$$x(z_{tp,1}) = \frac{\tan\theta_0}{\Gamma}\sinh(\Gamma z_{tp,1}) + x_0\cosh(\Gamma z_{tp,1}) = s\rho.$$

By using hyperbolic identities, we have

$$\frac{\tan\theta_0}{\Gamma}\left[\cosh^2(\Gamma z_{tp,1}) - 1\right]^{1/2} + x_0\cosh(\Gamma z_{tp,1}) = s\rho.$$

Solving the quadratic equation, we obtain

$$\cosh(\Gamma z_{tp,1}) = \frac{-s\rho x_0\Gamma^2 \pm \tan\theta_0\left[\tan^2\theta_0 + \Gamma^2\left(\rho^2 - x_0^2\right)\right]^{1/2}}{\tan^2\theta_0 - x_0^2\Gamma^2},$$

where it has been taken into account that $s^2 = 1$ for all cases. Therefore,

$$z_{tp,1} = \frac{1}{\Gamma}\operatorname{arccosh}\left\{\frac{-s\rho x_0\Gamma^2 \pm \tan\theta_0\left[\tan^2\theta_0 + \Gamma^2\left(\rho^2 - x_0^2\right)\right]^{1/2}}{\tan^2\theta_0 - x_0^2\Gamma^2}\right\}.$$

For a real-valued inverse hyperbolic cosine, its argument must be positive and equal or greater than unity. Therefore, and taking into account the value of s according to equation (B1), we will write:

$$
\begin{cases}
\text{if}\quad x_0 \geqslant 0 \Rightarrow z_{\text{tp},1} \\
\qquad =
\begin{cases}
\frac{1}{\Gamma}\operatorname{arccosh}\left(\frac{+\rho x_0 \Gamma^2 - G}{\tan^2\theta_0 - x_0^2\Gamma^2}\right) & \text{if } |\tan\theta_0| > |x_0|\,\Gamma \\
& \text{and } \tan\theta_0 < 0, \\
\frac{1}{\Gamma}\operatorname{arccosh}\left(\frac{-\rho x_0 \Gamma^2 + G}{\tan^2\theta_0 - x_0^2\Gamma^2}\right) & \text{rest of cases,}
\end{cases} \\
\text{if}\quad x_0 < 0 \Rightarrow z_{\text{tp},1} \\
\qquad =
\begin{cases}
\frac{1}{\Gamma}\operatorname{arccosh}\left(\frac{-\rho x_0 \Gamma^2 + G}{\tan^2\theta_0 - x_0^2\Gamma^2}\right) & \text{if } |\tan\theta_0| > |x_0|\,\Gamma \\
& \text{and } \tan\theta_0 > 0, \\
\frac{1}{\Gamma}\operatorname{arccosh}\left(\frac{+\rho x_0 \Gamma^2 - G}{\tan^2\theta_0 - x_0^2\Gamma^2}\right) & \text{rest of cases,}
\end{cases}
\end{cases}
$$
$$\tag{B2}$$

being

$$
G = \tan\theta_0 \left[\tan^2\theta_0 + \Gamma^2\left(\rho^2 - x_0^2\right)\right]^{1/2}.
$$

The previous result can be written compactly, leading to equation (32).

Appendix C. Ray path and ray half-period for bound skew rays

We calculate the ray path $z(r)$ after having substituted equation (1) into equation (38), obtaining

$$
z(r) = z_0 + \tilde{\beta}\int_{r_0}^{r}\left\{n_o^2\left[1 + 2\Delta\left(\frac{r'}{\rho}\right)^2\right] - \tilde{\beta}^2 - \tilde{l}^2\frac{\rho^2}{(r')^2}\right\}^{-1/2}\mathrm{d}r'
$$
$$
= z_0 + \tilde{\beta}\int_{r_0}^{r}\left[\left(n_o^2 - \tilde{\beta}^2\right)(r')^2 + \frac{n_o^2 2\Delta}{\rho^2}(r')^4 - \tilde{l}^2\rho^2\right]^{-1/2}r'\,\mathrm{d}r'.
$$

By rearranging the equation above, we have

$$
z(r) = z_0 + \frac{\tilde{\beta}\rho}{n_o\sqrt{2\Delta}}
$$
$$
\times \int_{r_0}^{r}\left[(r')^4 - \left(\tilde{\beta}^2 - n_o^2\right)\frac{\rho^2}{n_o^2 2\Delta}(r')^2 - \tilde{l}^2\frac{\rho^4}{n_o^2 2\Delta}\right]^{-1/2}r'\,\mathrm{d}r'.
$$
$$\tag{C1}$$

After the change of variable $\zeta' = (r')^2$,

$$
z(r) = z_0 + \frac{1}{2\Gamma}
$$
$$
\times \int_{\zeta_0}^{\zeta}\left[(\zeta')^2 - \left(\tilde{\beta}^2 - n_o^2\right)\frac{\rho^2}{n_o^2 2\Delta}\zeta' - \tilde{l}^2\frac{\rho^4}{n_o^2 2\Delta}\right]^{-1/2}\mathrm{d}\zeta',
$$
$$\tag{C2}$$

where we have replaced the first term of equation (C1) with Γ from equation (24). If we define the following parameters

$$
2\alpha^2 = \left(\tilde{\beta}^2 - n_o^2\right)\frac{\rho^2}{n_o^2 2\Delta}\quad\text{and}\quad \gamma^2 - \alpha^4 = \tilde{l}^2\frac{\rho^4}{n_o^2 2\Delta}\ ,
$$

and substitute them into equation (C2), then the latter reduces to

$$
z(r) = z_0 + \frac{1}{2\Gamma}\int_{\zeta_0}^{\zeta}\left[(\zeta')^2 - 2\alpha^2\zeta' - \left(\gamma^2 - \alpha^4\right)\right]^{-1/2}\mathrm{d}\zeta'
$$
$$
= z_0 + \frac{1}{2\Gamma}\int_{\zeta_0}^{\zeta}\left[\left(\zeta' - \alpha^2\right)^2 - \gamma^2\right]^{-1/2}\mathrm{d}\zeta'.
$$

This integral can be solved analytically after the change of variable $\psi' = \left(\zeta' - \alpha^2\right)/\gamma$. Consequently,

$$
z(r) = z_0 + \frac{1}{2\Gamma}\int_{\psi_0}^{\psi}\left[(\psi')^2 - 1\right]^{-1/2}\mathrm{d}\psi' = z_0 + \frac{1}{2\Gamma}\left.\operatorname{arccosh}\psi'\right|_{\psi_0}^{\psi}.
$$

Finally, by restoring the changes of variables inversely, we obtain the same expression of equation (39):

$$
z(r) = z_0 + \frac{1}{2\Gamma}\left.\operatorname{arccosh}\left(\frac{\zeta' - \alpha^2}{\gamma}\right)\right|_{\zeta_0}^{\zeta}
$$
$$
= z_0 + \frac{1}{2\Gamma}\left.\operatorname{arccosh}\left(\frac{(r')^2 - \alpha^2}{\gamma}\right)\right|_{r_0}^{r}.
$$
$$\tag{C3}$$

The ray half-period z_p is readily obtained from twice the axial distance (in absolute value) between a turning point (at $r = \rho$) and an adjacent inner caustic (at $r = r_{\text{ic}}$, where r_{ic} is calculated using equation (16)). Substitution of these radii at equation (C3) yields the same expression of equation (41):

$$
z_p = 2\,|z(\rho) - z(r_{\text{ic}})|
$$
$$
= \frac{1}{\Gamma}\left|\operatorname{arccosh}\left(\frac{\rho^2 - \alpha^2}{\gamma}\right) - \operatorname{arccosh}\left(\frac{r_{\text{ic}}^2 - \alpha^2}{\gamma}\right)\right|. \tag{C4}
$$

ORCID iDs

Joseba Zubia ⓘ https://orcid.org/0000-0002-9137-1733
Gotzon Aldabaldetreku ⓘ https://orcid.org/0000-0001-6217-6229
Gaizka Durana ⓘ https://orcid.org/0000-0002-1107-2400
María Asunción Illarramendi ⓘ https://orcid.org/0000-0002-7887-5435

References

[1] Snyder A W and Love J D 1983 *Optical Waveguide Theory* 1st edn (New York: Chapman and Hall) pp 6–119
[2] Ankiewicz A and Pask C 1977 The geometric optics approach to light acceptance and propagation in graded index fibers *Opt. Quantum Electron.* **9** 87–109
[3] Barrell K F and Pask C 1979 Geometric optics analysis of non-circular, graded index fibers *Opt. Quantum Electron.* **11** 237–51
[4] Szafraniec B and Briley B E 1990 Geometric optics analysis of modal propagation in graded-index cylindrical fiber *Appl. Opt.* **29** 1772–9

[5] Ghatak A G and Sauter E G 1989 The harmonic oscillator problem and the parabolic index optical waveguide: I. Classical and ray optic analysis *Eur. J. Phys.* **10** 136–43

[6] Ghatak A G, Sharma E and Kompella J 1988 Exact ray paths in bent waveguides *Appl. Opt.* **27** 3180–4

[7] Zubia J, Aldabaldetreku G, Durana G, Arrue J and Jiménez F 2008 Light propagation in multi-step index optical fibers *Laser Photonics Rev.* **2** 182–202

[8] Berganza A, Aldabaldetreku G, Zubia J and Durana G 2010 Ray tracing analysis of crosstalk in multi-core polymer optical fibers *Opt. Express* **18** 22446–61

[9] Lachance R L and Bélanger P-A 1991 Modes in divergent parabolic graded-index optical fibers *J. Light Technol.* **9** 1425–30

[10] Ung B, Wang L, Brunet C, Vaity P, Jin C, Rusch L A, Messaddeq Y and LaRochelle S 2014 Inverse-parabolic graded-index profile for transmission of cylindrical vector modes in optical fibers *Optical Fiber Communication Conference 2014* (*San Francisco, California United States, 9–13 March 2014*) *Proc. OFC2014 Optical Fiber Communication Conf.* (https://doi.org/10.1364/OFC. 2014.Tu3K.4)

[11] Ung B, Vaity P, Wang L, Messaddeq Y, Rusch L A and LaRochelle S 2014 Few mode fiber with inverse parabolic graded-index profile for transmission of OAM-carrying modes *Opt. Express* **22** 18044–55

[12] Matejec V, Chomat M, Kasik I, Ctyroky J, Berkova D and Hayer M 1998 Inverted graded-index fiber structures for evanescent-wave chemical sensing *Sens. Actuators* B **51** 340–7

[13] Tsukada K, Asakura K and Nihei E 2014 Fabrication and light branching of negative type GI plastic optical fiber *Proc. POF 2014–23rd Int. Conf. on Plastic Optical Fibers*

[14] Ayesta I, Azkune M, Arrospide E, Arrue J, Illarramendi M A, Durana G and Zubia J 2019 Fabrication of active polymer optical fibers by solution doping and their characterization *Polymers* **11** 52

[15] Matejec V, Kasik I, Chomat M, Ctyroky J, Berkova D and Hüttel I 1999 Modified inverted graded–index fibers for evanescent-wave chemical sensing *Proc. SPIE* **3860** 443–51

[16] Chomat M, Berkova D, Matejec V, Ctyroky J, Kasik I, Gagnaiere H, Trouillet A and Bardin F 1999 Detection of refractive-index changes by using a sensing fiber with an inverted parabolic index profile *Proc. SPIE* **3860** 179–89

[17] Bardin F, Kasik I, Trouillet A, Matejec V, Gagnaire H and Chomat M 2002 Surface plasmon resonance sensor using an optical fiber with an inverted graded index-profile *Appl. Opt.* **41** 2514–20

[18] Chomat M, Berkova D, Matejec V, Kasik I and Kuncova G 2003 The effect of hydrodynamic conditions on the detection of aqueous solutions of toluene by means of an inverted graded-index fiber *Sens. Actuators* B **90** 151–6

[19] Nasirifar R, Danaie M and Dideban A 2021 Surface plasmon resonance biosensor using inverted graded index optical fiber *Photon. Nanostruct: Fundam. Appl.* **44** 100916

[20] McIntosh K, Yamada N and Richards B 2007 Theoretical comparison of cylindrical and square-planar luminescent solar concentrators *Appl. Phys.* B **88** 285–90

[21] Wang T, Yu B, Chen B, Hu Z, Luo Y, Zou G and Zhang Q 2013 A theoretical model of a cylindrical luminescent solar concentrator with a dye-doping coating *J. Opt.* **15** 055709

[22] Correia S F H, Lima P P, André P S, Sá Ferreira M R and Dias Carlos L A 2015 High-efficiency luminescent solar concentrators for flexible waveguiding photovoltaics *Sol. Energy Mater. Sol. Cells* **138** 51–57

[23] Arrospide E, Illarramendi M A, Ayesta I, Guarrotxena N, García O, Zubia J and Durana G 2021 Effects of fabrication methods on the performance of luminescent solar concentrators based on doped polymer optical fibers *Polymers* **13** 424

[24] Grandes J, Illarramendi M A, Arrospide E, Bikandi I, Aramburu I, Guarrotxena N, Garcia O and Zubia J 2022 Temperature effects on the emission of polymer optical fibers doped with Lumogen dyes *Opt. Fiber Technol.* **72** 102980

[25] Born M and Wolf E 1999 *Principles of Optics* 7th edn (New York: Cambridge University Press) pp 116–39

[26] Holm D D 2012 Fermat's principle and the geometric mechanics of ray optics *Summer School Lectures* (Canada: Fields Institute Toronto)

[27] Kanh W K and Yang S 1982 Application of Hamiltonian methods to analogous problems in optics: optical fibers *Proc. SPIE* **358** 39–46

[28] Black R J and Ankiewicz A 1985 Fiber-optic analogies with mechanics *Am. J. Phys.* **53** 554–63

[29] Abramowitz M and Stegun I A 1964 *Handbook of Mathematical Functions with Formulas, Graphs, and Mathematical Tables* (New York: Dover Publications, Inc.)